PCCP

View Online

Dynamic Article Links

Cite this: *Phys. Chem. Chem. Phys.*, 2011, **13**, 8549–8559

www.rsc.org/pccp

PAPER

Towards the complete experiment: measurement of $S(^1D_2)$ polarization in correlation with single rotational states of CO(*J*) from the photodissociation of oriented $OCS(v_2 = 1|JlM = 111)$

M. Laura Lipciuc,[a] T. Peter Rakitzis,[b] W. Leo Meerts,[ac] Gerrit C. Groenenboom[c] and Maurice H. M. Janssen*[a]

Received 26th November 2010, Accepted 8th March 2011
DOI: 10.1039/c0cp02671a

In this paper we report slice imaging polarization experiments on the state-to-state photodissociation at 42 594 cm^{-1} of spatially oriented $OCS(v_2 = 1|JlM = 111) \rightarrow CO(J) + S(^1D_2)$. Slice images were measured of the three-dimensional recoil distribution of the $S(^1D_2)$ photofragment for different polarization geometries of the photolysis and probe laser. The high resolution slice images show well separated velocity rings in the $S(^1D_2)$ velocity distribution. The velocity rings of the $S(^1D_2)$ photofragment correlate with individual rotational states of the CO(*J*) cofragment in the $J_{CO} = 57$–65 region. The angular distribution of the $S(^1D_2)$ velocity rings are extracted and analyzed using two different polarization models. The first model assumes the nonaxial dynamics evolves after excitation to a single potential energy surface of an oriented $OCS(v_2 = 1|JlM = 111)$ molecule. The second model assumes the excitation is to two potential energy surfaces, and the OCS molecule is randomly oriented. In the high *J* region ($J_{CO} = 62$–65) it appears that both models fit the polarization very well, in the region $J_{CO} = 57$–61 both models seem to fit the data less well. From the molecular frame alignment moments the *m*-state distribution of $S(^1D_2)$ is calculated as a function of the CO(*J*) channel. A comparison is made with the theoretical *m*-state distribution calculated from the long-range electrostatic dipole–dipole plus quadrupole interaction model. The $S(^1D_2)$ photofragment velocity distribution shows a very pronounced strong peak for $S(^1D_2)$ fragments born in coincidence with $CO(J = 61)$.

I. Introduction

Polarization of the electronic angular momentum of atomic photofragments can be induced by photodissociation of molecules with polarized light.[1] Measurement of the photofragment angular momentum polarization and **v**–**J** correlation, where **v** is the laboratory velocity of the fragment, can provide detailed insight into the dynamics of the photodissociation process.[2–4] The **v**–**J** correlation, together with the measurement of the recoil anisotropy parameter,[5] can be used to determine the symmetry of excited states, the (anisotropic) shape of dissociative surfaces, the nature of avoided crossings, and the influence of the long-range interaction forces.[3,4,6–8] Photofragment imaging methods[9–17] are powerful techniques for the study of photodissociation processes. The directly measured or inverted three-dimensional (3D) recoil distribution of photofragments provides the angular and velocity distribution of the fragments. Detection of the fragment with varying polarization of the probe light can reveal the (potentially induced) electronic or rotational anisotropy of the fragment. The application of imaging to measure anisotropy of angular momentum was demonstrated shortly after the invention of ion imaging[9] in a study of the alignment of the rotational angular momentum of the methyl fragment from the photodissociation of methyl iodide.[18]

The photodissociation of carbonyl sulfide (OCS) has been extensively investigated in the wavelength region of 222–248 nm,[14,19–35] which is near the maximum and on the red side of the absorption band.[36,37] During the last five years there have been many new studies published on the photodissociation of OCS and these high quality experimental data have turned the OCS molecule into a benchmark system for photodissociation studies of triatomic molecules. Following absorption of a UV photon around 230 nm $OCS(X^1\Sigma^+)$ dissociates into S(95% $^1D_2$, 5% $^3P_2$) and $CO(X^1\Sigma^+)$ photofragments.[20] The CO fragments are released in the vibrational ground state but are rotationally highly excited. In the $X^1\Sigma^+$ ground electronic state the OCS molecule is linear. As reported

[a] *LaserLaB Amsterdam and Department of Chemistry, Vrije Universiteit, de Boelelaan 1083, 1081 HV Amsterdam, The Netherlands. E-mail: mhmj@chem.vu.nl*
[b] *Department of Physics, University of Crete, and IESL-FORTH, P.O. 1527, 71110, Heraklion, Greece*
[c] *Institute for Molecules and Materials, Radboud University Nijmegen, Heyendaalseweg 135, 6525 AJ Nijmegen, The Netherlands*

by Suzuki *et al.*[22] there are three electronic states correlating with the $S(^1D)$ + $CO(X^1\Sigma^+)$ dissociation channel, the $1^1\Sigma^+$, $1^1\Pi$ and $1^1\Delta$ states, and one electronic state, the $1^1\Sigma^-$ state, correlating with the $S(^3P)$ + $CO(^3\Pi^+)$ dissociation channel. Transitions from the ground electronic state to these electronically excited states are forbidden when the molecule is linear but become allowed in the bent geometry (C_s). Away from linearity the $1^1\Delta$ electronic state splits into the $2^1A'$ and $2^1A''$ Renner–Teller pairs, the $1^1\Pi$ splits into $3^1A'$ and $3^1A''$ states, the $1^1\Sigma^+$ becomes $1^1A'$ and $1^1\Sigma^-$ becomes the $1^1A''$ state. At 230 nm only the $2^1A'(1^1\Delta)$ and $1^1A''(1^1\Sigma^-)$ surfaces are energetically accessible through parallel ($2^1A'$) and perpendicular ($1^1A''$) transitions. It was reported in the study by Suzuki *et al.*[22] that nonadiabatic transitions from the $2^1A'$ electronically excited state to the $1^1A'$ electronic ground state take place during dissociation of OCS and this mechanism is believed to cause a bimodal rotational distribution of the CO(J) fragments. Recently,[33] state-to-state cross section data were published for photodissociation of ground state and vibrationally excited OCS(ν_2 = 0,1,2), reporting the strong enhancement of the absorption cross section with increasing excitation of the bending mode of OCS. This effect was interpreted as reflecting the strong increase of the transition dipole moment with increasing OCS bending angle. Furthermore, calculations of the transition dipole moment[22] showed that the parallel (in plane) component is increasing much faster than the perpendicular component when the OCS bending angle increases from 0 to 30°. This different change of the strength of the parallel and perpendicular dipole moment with OCS bending angle was attributed to cause the different β-parameters for ground state *versus* vibrationally excited OCS(ν_2 = 1).[26] Recently, Brouard *et al.*[34] proposed the transition dipole moment to make an angle of 65°–80° to the linear OCS axis. However, this very large angle seems to be at odds with the *ab initio* calculations by Suzuki *et al.*[22] The experiments by Brouard and coworkers were performed at a photolysis wavelength of 248 nm which is far out in the red wing of the absorption spectrum, and perhaps they were more sensitive to photolysis from higher vibrationally excited states of OCS like ν_2 = 1,2. Furthermore, the state-to-state experiments using spatially oriented OCS(v_2 = 1|J|M = 111) concluded that the angle between the direction of the transition dipole moment and the direction of the permanent dipole moment, which is along the linear OCS axis, is about 30°.[14,28] Very recently, Danielache *et al.*[38] reported new *ab initio* calculations on the potential energy surfaces and the transition dipole moment function of OCS and the various isotopologues.

It has been reported before[23,25,30,34,39,40] that the $S(^1D_2)$ photofragment electronic angular momentum is anisotropic. Siebbeles *et al.*[41] developed a full quantum treatment of the photodissociation of diatomic molecules in the axial recoil limit, and Vasyutinskii and coworkers[42–44] further developed this treatment and recently extended the formalism to predissociating and bending triatomic systems.[45–47] Rakitzis and Zare[48] introduced a similar description of photofragment polarization from diatomic photodissociation in terms of the molecular-frame polarization parameters $a_q^{(k)}(p)$. More recently, Rakitzis and coworkers have extended this formalism to describe photofragment polarization from the photodissociation of polyatomic molecules,[49,50] oriented molecules,[51] and rotating parent molecules.[52] It was also shown that both formalisms are fully equivalent and the various alignment parameters can be related by simple expressions, see *e.g.* ref. 4 and 50 for a thorough recent review of this equivalence.

Rakitzis *et al.*[25] interpreted their results for the $S(^1D_2)$ alignment after photolysis of OCS at 223 nm in terms of incoherent ($a_0^{(k)}(\|)$ and $a_q^{(k)}(\perp)$) and coherent ($a_1^{(k)}(\|,\perp)$) molecular frame anisotropy moments for the fast and slow $S(^1D_2)$ + $CO(X^1\Sigma^+)$ channels. These values are in good agreement with the values reported by Kim *et al.*[23] and Brouard *et al.*[34]

Using a quantum state-selected molecular beam and velocity map imaging van den Brom *et al.*[30] reported values of the alignment moments for photolysis of quantum state-selected OCS at 223 nm and 230 nm. The m-state distribution can be calculated directly from the $a_q^{(k)}(p)$ alignment moments.[48] For the OCS photolysis the $m = \pm 1$ state seems to carry most of the population for both fast and slow channel.[25,30,34] However, the interpretation of these $a_q^{(k)}(p)$ parameters (which describe axial-recoil diatomic photodissociation dynamics) is not straightforward for the nonaxial recoil photodissociation of OCS; therefore, in this paper, we use the more recently developed $a_q^{(k)}(s)$ formalism for polyatomic nonaxial-recoil photodissociation.[49]

The long-range dipole–dipole and dipole–quadrupole interaction model was introduced by Teule *et al.*[7] to explain the changing m-state population of $O(^1D_2)$ with correlated $N_2(J)$ from the photolysis of the isoelectronic molecule N_2O around 205 nm. They suggested that the N_2O dissociation takes place adiabatically on the $2A'$ and $1A''$ surfaces until, at large separation between the fragments, the m-state population derives from the long-range dipole–quadrupole and quadrupole–quadrupole interaction. This long-range model was subsequently used to interpret polarization studies in various other triatomic systems.[53–56] Very recently, a new full theoretical study on the validity of the long-range model was performed by Groenenboom and coworkers.[57] Preliminary conclusions from this full theoretical study are that the experimental trend[7] that for $O(^1D_2)$ born in coincidence with low N_2 rotational levels the population of $|M| = 1$ sub-levels is preferred, while for the highest rotational levels of N_2, the $O(^1D_2)$ products are preferentially formed with $M = 0$, can be qualitatively accounted for by the long-range electrostatic model. However, it seems that the location at which the populations are formed is at a somewhat closer distance and the approximation of the real potentials by the long-range dipole–dipole plus dipole–quadrupole interaction is not sufficient. Therefore, more theoretical work is needed to account properly for the relative contributions of the parallel and perpendicular components of the transition strength to the absorption.[57]

In this paper we report new experimental data on the polarization of the $S(^1D_2)$ photofragment following the photodissociation of state-selected OCS(v_2 = 1|J|M = 111) at 42 594 cm^{-1}. Recent technological developments using high-resolution slice imaging[16] make it possible to measure well-separated rings in the slice images of the $S(^1D_2)$ fragment correlating with individual rotational states of the CO(J) cofragment.[32] In section II we first discuss the relevant

theoretical framework to analyze and interpret our data. In Section III we give a brief description of the experimental set-up and in section IV we present our experimental results. In section V we discuss our results and summarize our main conclusions.

II. Theory

The S(^{1}D$_2$) photofragments resulting from the photolysis of OCS have an anisotropic angular momentum distribution, which is sensitive to the polarization directions of the photolysis and probe lasers, but also, to some extent, to the direction of the ion extraction field that is used to image the photofragments. This ion extraction field will also orient and align the OCS($v_2 = 1|J|M = 111$) quantum state that is selected by the hexapole.

Recently, Rakitzis and Janssen presented the molecular-frame and laboratory-frame ionization probability of photofragments from the photodissociation of oriented parent molecules *via* a single dissociative state, in terms of the molecular-frame $a_q^{(k)}$ polarization parameters.[51] They showed that, for experimental geometries where the orientation field is perpendicular to the imaging plane of the detector, as is the case in our experiment, the effect of the orientation field on the photofragment angular distributions is small.

We analyze the experimental signals using two different models. The first is the single-surface model[51] for oriented or aligned parent molecules, the second is a two-surface model for isotropic parent molecules, described by Rakitzis and Alexander,[49] for which the molecular-frame photofragment ionization probability is expressed in terms of the more general $a_q^{(k)}$ parameters[49,58]

$$\begin{aligned} I \propto 1 + c\beta C_0^2(\theta) + s_2\{A_0^2(\mathrm{iso})C_0^2(\Theta) + \\ cA_0^2(\mathrm{aniso})[C_0^2(\Theta)C_0^2(\theta)] + cA_1^2[C_1^2(\Theta)C_1^2(\theta)]\cos\Phi + \\ cA_2^2[C_2^2(\Theta)C_2^2(\theta)]\cos 2\Phi\} + s_4\{A_0^4(\mathrm{iso})C_0{}^4(\Theta) + \\ cA_0^4(\mathrm{aniso})[C_0^4(\Theta)C_0^2(\theta)] + cA_1^4[C_1^4(\Theta)C_1^2(\theta)]\cos\Phi + \\ cA_2^4[C_2^4(\Theta)C_2^2(\theta)]\cos 2\Phi\}, \end{aligned} \quad (1)$$

where $A_q^{(k)}$ are the molecular frame polarization parameters ($k = 2$ and 4), $C_q^{(k)}(\theta)$ are the modified spherical harmonics, Θ is the polar angle between the recoil direction of the photofragments and the probe laser polarization, Φ is the azimuthal angle of the pump and probe polarization with the recoil velocity of the photofragments and θ is the angle between the photolysis laser polarization and the recoil direction of the S(^{1}D$_2$) fragments. The constant $c = 1$ when the photolysis laser is linearly polarized. We will only present results here for linearly polarized photolysis light. The s_2 and s_4 are the line strength detection factors for (2+1) REMPI of the S(^{1}D$_2$) state and take on values $s_2 = -5/7$ and $s_4 = -48/7$ when the S(^{1}D$_2$) is detected *via* the ^{1}P$_1$ resonant intermediate, and values $s_2 = 40/49$ and $s_4 = -36/49$ when the ^{1}F$_3$ state is the resonant intermediate.[49] We assume here that the one photon ionization step from the intermediate state is not sensitive to the polarization of the probe laser.[59] All the above values for the s_k ($k = 2$ and 4) parameters are for a linearly polarized probe laser.

We note that eqn (1) forms a complete basis for the description of experimental signals from photofragment angular momentum polarization (up to $k = 4$, using linearly polarized photolysis and probe light), as does the bipolar moment formalism.[60] Recently, Vasyutinskii and coworkers[46,47] have shown how the parameters of such a general expansion can be calculated, for a general range of photodissociation mechanisms, thus opening the direction of the quantitative description of angular momentum polarization from polyatomic photodissociation.

We use the velocity map slice imaging technique to measure directly a cut through the three-dimensional angular distribution of the photofragment. The molecular frame angles can be expressed in terms of laboratory frame angles.[61] For our slice imaging geometry with a probe laser polarization either parallel to the polarization of the photolysis or perpendicular to the plane of the 3D-slice we can express the molecular frame ionization probability in terms of a single laboratory frame angular coordinate, θ, the angle between the photolysis laser polarization and the recoil direction of the S(^{1}D$_2$) fragment. For each pump–probe laser geometry eqn (1) becomes an expansion of second, fourth or sixth order Legendre polynomials P$_l$(cos θ)

$$I(\theta) \propto 1 + \beta_2 P_2(\cos\theta) + \beta_4 P_4(\cos\theta) + \beta_6 P_6(\cos\theta) \quad (2)$$

where β_2, β_4 and β_6 are the expansion coefficients.

Using the molecular-frame to laboratory-frame transformation (eqn (17) and (18) in ref. 49), eqn (1) can be expressed in the form of eqn (2), in terms of the single coordinate θ, and β_l in terms of $A_q^{(k)}$ parameters. Explicit expressions for the β_l are given for the experimental geometry where the probe and photolysis polarization directions are parallel to each other and the imaging plane of the detector.[58]

The maximum order of Legendre polynomials that will appear in the expansion in eqn (2) is given by the value $2(m + n)$, where m is the number of photolysis photons (in this experiment $m = 1$) and n is the number of probe photons to the intermediate resonant state (in this experiment $n = 2$). The expansion is terminated at the sixth order if both laser polarizations are parallel to each other and parallel to the detector slice plane. If the polarization of the photolysis laser is parallel to the detector slice plane and the polarization of the probe laser is perpendicular to the detector slice plane direction the expansion will terminate at the second order. If the polarization of the photolysis laser is perpendicular to the detector slice plane and the polarization of the probe laser is parallel to the detector slice plane the expansion will terminate at the fourth order. The experimentally determined β_l ($l = 2,4,6$) parameters contain information about the anisotropy parameter β and the photofragment alignment moments $A_q^{(k)}$. As demonstrated by Rakitzis[58] several pump–probe laser polarization geometries can be used in order to measure completely the photofragment alignment.

III. Experimental

The experimental setup has been described in great detail before.[16,26,62,63] Here we give only a brief description of the experimental conditions. A mixture of 20% OCS seeded in Ar is supersonically expanded through a pulsed nozzle (General Valve solenoid pulsed valve) and skimmed before it enters a

second buffer chamber containing a removable beam stop. The beam stop is used to enhance the selectivity of the hexapole in the third chamber. The hexapole focuses OCS(v_2 = 1|JlM = 111) molecules onto a 1 mm in diameter conically shaped hole in the repeller plate of the ion optics. The rotationally state-selected OCS(v_2 = 1|JlM = 111) molecules are intersected by two counter propagating UV laser beams. The OCS molecules are photolyzed by a 42 594 cm^{-1} photon. The S($^1D_2$) fragments are detected by (2+1) REMPI ionization *via* the $^1P_1$ and $^1F_3$ resonant intermediate states. The probe laser was set at 291.476 nm (vacuum wavelength) for the detection of S($^1D_2$) *via* the $^1P_1$ intermediate state and at 288.179 nm (vacuum wavelength) for the detection of S($^1D_2$) *via* the $^1F_3$ intermediate state. The S ions are velocity mapped on a position sensitive detector (MCP/Phosphor/CCD camera) after passing a time-of-flight tube. The MCP detector is gated with a homebuilt fast HV pulser with an effective gain width of the slice of about 12 ns in order to detect only the central part of the sulfur ion cloud. The light from the phosphor screen is imaged by a 2048 by 2048 pixels large frame CCD camera. To obtain the position of the individual ion events on the phosphor screen we used centroiding techniques to read out the CCD camera.[32,64]

IV. Results

Data was measured at several pump–probe laser geometries through both the $^1P_1$ and the $^1F_3$ two photon resonant intermediate states. These geometries are VV, VH, HV and HH where the first letter indicates the polarization of the pump laser and the second letter indicates the polarization of the probe laser. The label V is for the geometry with the polarization of the laser vertical and in the plane of the slice image, the label H is for the geometry with the polarization of the laser horizontal and perpendicular to the slice imaging plane. From the data taken with these laser geometries the alignment moments of the S($^1D_2$) can be obtained. Other data was taken for a geometry with the polarization of the photolysis laser at an angle of 45° with respect to the molecular beam axis and the polarization of the probe laser either linear (V and H) or circular polarized (C). These experiments were performed to probe the orientation of the angular momentum of the S atom and the results will be reported elsewhere. In Fig. 1 we present a slice image of S($^1D_2$) detected through the $^1F_3$ resonant intermediate after photolysis of single quantum state-selected OCS(v_2 = 1|JlM = 111) at 42 594 cm^{-1}. The image was recorded in the VH laser geometry, *i.e.* with the probe laser perpendicular to the slice imaging plane. In the image clearly separated velocity rings of the S photofragments, correlating with single rotational states of the CO(J) cofragment, can be observed. To obtain the velocity distribution of the image shown in Fig. 1 the intensity of each ring at a constant radius ρ is integrated over the angular range by multiplying the ion events at each pixel by $\rho \sin\theta$, where θ is the angle between the recoil velocity and the vertical direction of the polarization of the photolysis laser.

In Fig. 2 two velocity distributions of the S($^1D_2$) fragment are shown, one for detection *via* the $^1F_3$ resonant intermediate state and one for detection *via* the $^1P_1$ resonant intermediate

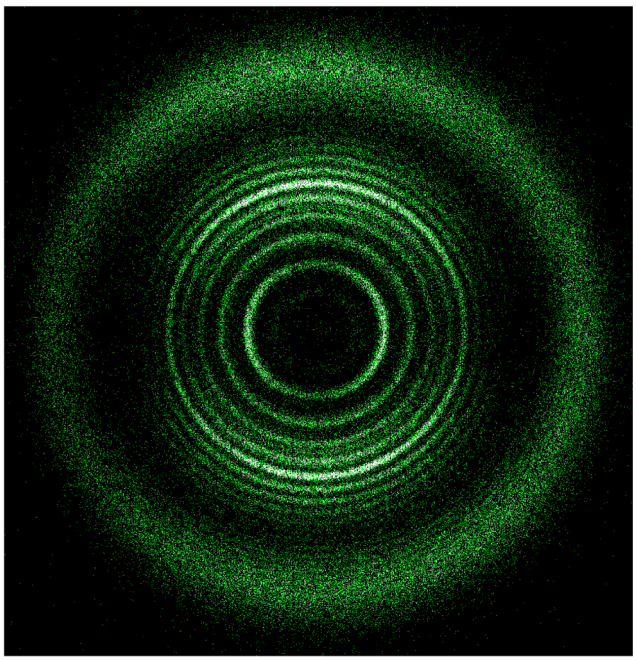

Fig. 1 Slice image of S($^1D_2$) from the photolysis of OCS(v_2 = 1|JlM = 111) at 42 594 cm^{-1}. The S($^1D_2$) photofragment is probed *via* (2+1) REMPI through the $^1F_3$ resonant intermediate. The pump and probe lasers are counterpropagating with the polarization of the pump laser vertical and in the plane of the slice image and the polarization of the probe laser perpendicular to the slice image plane, *i.e.* VH geometry. The 'peak' image shown (size 1095 by 1134 pixels), is an event-counted date file of many raw images. Each raw image is read out at a rate of about every 5 laser shots (the lasers run at 10 Hz). The spots of single ion events are located by a fast computer routine. The pixel with the highest intensity of every located ion spot is taken to represent the location (x,y) of that event. In the 'peak' image the intensity of a (x,y) pixel corresponds to the total number of S($^1D_2$) events at that position summed over many laser shots. In total, the 'peak' image shown here has 192 033 single ion events. To visualize better the highly pixelated 'peak' image we clipped the intensity scale.

state. The calibration of the S($^1D_2$) velocity was done on the strong peak in the high J_{CO} region which we assigned to S($^1D_2$) produced in correlation with CO(J = 61). A dissociation energy for OCS(v_2 = 0|J = 0) → CO(J = 0) + S($^1D_2$) of D_0 = 34 608 cm^{-1} was used as determined recently with high accuracy.[32] The photolysis energy of 42 594 cm^{-1}, a rovibrational energy for the OCS(v_2 = 1|JlM = 111) state of 520.6 cm^{-1}, and a rotational energy of CO(J = 61) of 7184.1 cm^{-1} were used.

The bimodal structure of the CO(J) rotational distribution reported before[19,21–23,26–27,34] is very clearly observed in Fig. 2. It has been shown[16,32] that the velocity resolution of slice images can be enhanced by directing the recoil kick of the ionization step by proper orientation of the polarization of the probe laser. In the case of OCS the best velocity resolution is obtained when the polarization of the probe laser is perpendicular to the slice imaging plane. The velocity resolution in Fig. 2 is better for detection through the $^1F_3$ resonant intermediate, panel (b), compared to detection *via* the $^1P_1$ intermediate, panel (a). However, the expected recoil kick from the electron ejection is 16.2 m s^{-1} for detection through the $^1F_3$, slightly

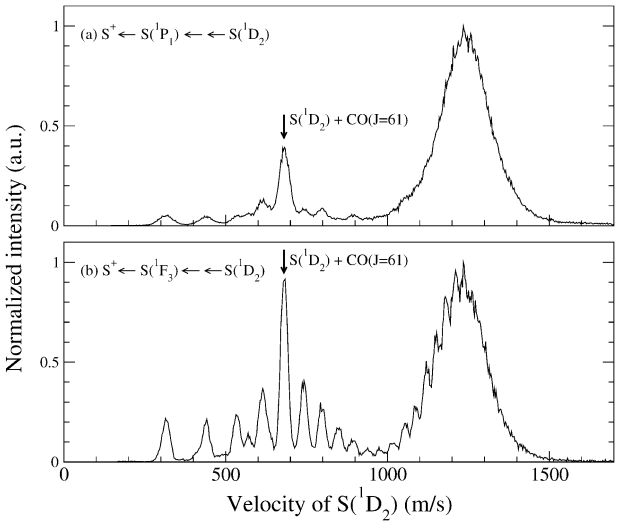

Fig. 2 Velocity distributon of $S(^1D_2)$ photofragments after photolysis of OCS(v_2 = 1|JlM = 111) at 42 594 cm^{-1}. For the detection of $S(^1D_2)$ photofragments we used the $^1P_1$ level as the resonant intermediate (panel a) or the $^1F_3$ level (panel b). Both spectra were from images taken in the VH geometry. The CO(J) rotational structure is clearly visible in the $S(^1D_2)$ velocity distribution. The spectra are fully resolved in the high J_{CO} region, especially when the $^1F_3$ state is used as an intermediate. The most intense peak in the slow channel, which corresponds to the $S(^1D_2)$ + CO(J = 61), is indicated.

larger than the expected kick of 15.7 m s^{-1} for detection through the $^1P_1$. This may be the result of an angular anisotropy of the electron ejection in the photoionization of the different M-levels of the intermediate resonant state, which are populated by a two photon excitation of an anisotropic $S(^1D_2)$ state.

The intensity ratio between the fast channel and the slow channel is very different when the $S(^1D_2)$ is detected *via* $^1P_1$ or *via* $^1F_3$. This is because the detection efficiency is sensitive to the alignment moments and the s_2 and s_4 line strength factors (see eqn (1)). The line strength factors are different for the two REMPI detection schemes and the alignment present in each $S(^1D_2)$ + CO(J) channel is therefore reflected in the overall signal strength.[58] This explains the strong change in the relative intensity ratio between the low J and high J channels when detecting *via* the $^1F_3$ or $^1P_1$ intermediate level, as is observed in Fig. 2.

Two raw data images and blow-ups of the upper part of each image of $S(^1D_2)$ detected *via* the $^1P_1$ resonant intermediate after photolysis of OCS(v_2 = 1|JlM = 111) at 42 594 cm^{-1} are shown in Fig. 3. The laser geometry was VH for the image in panel (a) and VV for the image in panel (c). These two geometries lead to very different angular distributions in both the slow and fast channel. In Fig. 4 and 5 we show the angular distribution of six selected velocity rings of $S(^1D_2)$ correlating to individual rotational states of CO(J) with J_{CO} = 65, 63, 61, 60, 59, 57, when the probe laser geometry changes from horizontal (H), panel (a) in Fig. 4 and 5, to vertical (V), panel (b) in Fig. 4 and 5. The solid lines in Fig. 4 and 5 are fits to the experimental data using the expression of eqn (2), see also below.

It is very clear that the angular distribution of $S(^1D_2)$ changes with the rotational state of the correlated CO(J) fragment. In VH geometry for the slower S-atoms correlating with highest CO(J), J = 61–65, the angular distribution changes from a perpendicular type of distribution for J_{CO} = 65 to a more parallel type of distribution for J_{CO} = 61. This strong reduction in the β parameter for fast rotating and slow moving CO fragments is attributed to a strong increase of the ratio of the tangential velocity and axial velocity of fragments with increasing CO(J), and was reported and discussed before by our group in the context of changing the photolysis energy when probing a single CO(J).[32]

For the VV geometry strong changes and a richly modulated angular distribution of $S(^1D_2)$ is observed with changing CO(J). For J_{CO} = 60, 59 and 57, the intensity of $S(^1D_2)$ is peaking more at 45° with respect to the vertical direction (clover-like distribution of intensity) in the VV geometry, and when J increases to higher J up to J = 65 the intensity moves from peaking near the vertical (0 and 180 degrees) to peaking near 90 degrees. Especially for J = 61 the $S(^1D_2)$ distribution in VV geometry peaks very strongly around (0,180) degrees and changes very strongly to a clover-like distribution for J = 60 (also very visible in the raw data of Fig. 3).

The angular distributions of $S(^1D_2)$ fragments at different velocities correlating to different CO(J) states were extracted from the slice images. The angular intensity distribution centered around the most probable velocity for each velocity peak, as determined from the radial velocity distribution spectra, was integrated within the FWHM of each velocity peak and fitted to the expression of eqn (2). In Table 1 we present the β_2, β_4 and β_6 Legendre polynomial coefficients obtained from the angular distributions in the VV, VH and HV geometries when the sulfur atom detection is through the $^1P_1$ resonant intermediate and in the VV and VH geometries when the S-atom detection is through the $^1F_3$ resonant intermediate. The slow channel is fully resolved so we report the Legendre coefficients for individual $S(^1D_2)$ + CO(J) channels. For the fast channel the individual $S(^1D_2)$ + CO(J) peaks are not well separated and we have chosen a single position at the peak of the broad distribution to extract the angular distribution.

In Table 1 we also present the β parameter as obtained from a separate experiment but detecting CO(J) photofragments in individual rotational states. For this separate experiment we kept the photolysis wavelength the same as for the experiment detecting the S fragment. The CO(J) fragments were detected by (2+1) REMPI in several rotational states (J_{CO} = 57–65) with the polarization geometry as VV or VH. To extract the true β parameter from the measured CO(J) slice images we need to correct for the small effect of alignment in our preparation of OCS(v_2 = 1|JlM = 111) parent molecules. Note that we ignore product CO(J) angular momentum, as the Q-branch detection is largely insensitive to product alignment.[23] The OCS(v_2 = 1|JlM = 111) molecules have both bond alignment and bond orientation along the TOF-axis, with the sulfur pointing towards the repeller plate and the oxygen pointing towards the extractor plate in our ion lens. For nonaxial recoil, which is the case for OCS photolysis near

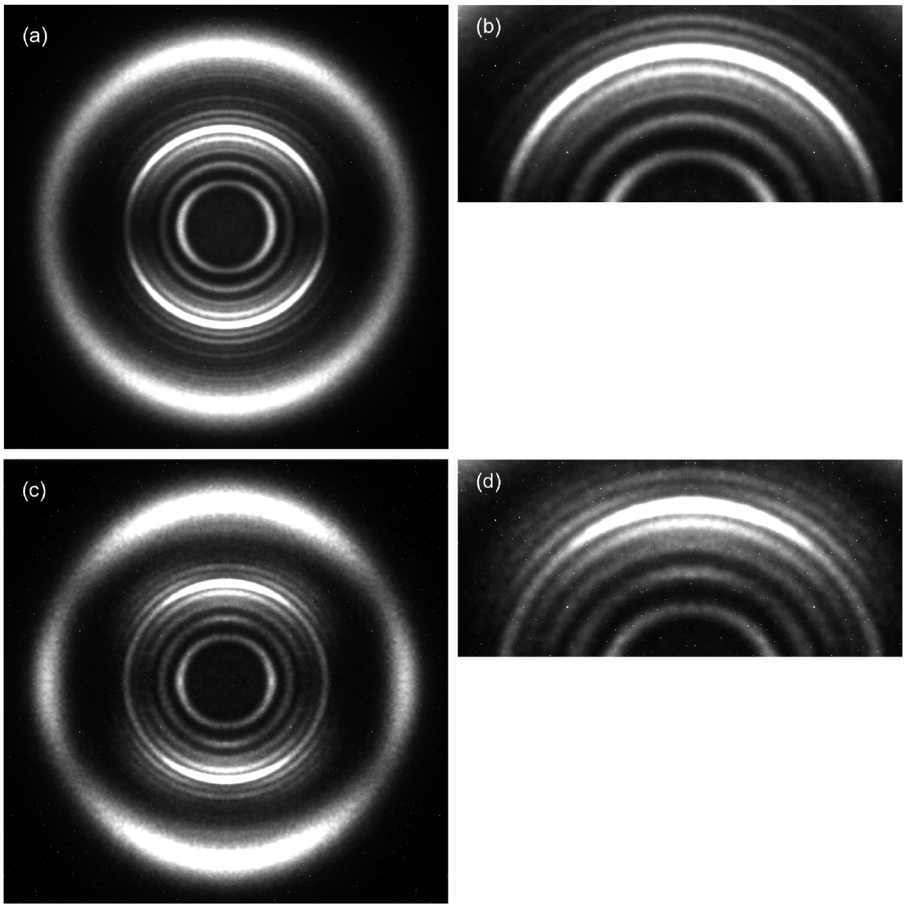

Fig. 3 Raw data images of S(^{1}D$_2$) photofragments after photolysis of OCS(v_2 = 1|JlM = 111) at 42 594 cm^{-1}. The S(^{1}D$_2$) photofragment is probed *via* (2 + 1) REMPI with the ^{1}P$_1$ level as resonant intermediate. The image in panel (b) is a cut of (630 by 280) pixels of the (1200 by 1200) pixels image in panel (a). The image in panel (d) is a cut of (630 by 280) pixels of the (1200 by 1200) pixels image in panel (c). In panels (a–b) the polarization of the pump laser was vertical and in the plane of the image and the polarization of the probe laser was horizontal (VH geometry) and perpendicular (normal) to the plane of the image. In panels (c–d) the polarizations of both pump and probe laser were vertical (VV geometry). Note how the angular distribution of individual rings in the high J_{CO} region and of the slow J_{CO} channel changes when the polarization of the probe laser is changed from horizontal to vertical.

230 nm, the angular distribution will depend on the degree of alignment of the parent molecule[61,65]

$$I(\theta) = 1 + \left[\frac{2P_2(\cos\chi) + \frac{3}{4}\frac{c_2 \sin^2\chi \sin^2\alpha_d}{1+2c_2P_2(\cos\alpha_d)}}{1 - \frac{3}{4}\frac{c_2 \sin^2\chi \sin^2\alpha_d}{1+2c_2P_2(\cos\alpha_d)}}\right] P_2(\cos\theta). \quad (3)$$

where χ is the angle between the transition dipole moment $\vec{\mu}$ and the recoil direction $\vec{v}$, θ is the angle between the photolysis laser polarization and the recoil direction, α_d is the angle between the permanent dipole moment $\vec{\nu}$ and the recoil direction. For the (v_2 = 1|JlM = 111) state the coefficient which describes the alignment of the permanent dipole moment, c_2 = 1/4 and the angle $\alpha_d = \chi + 30^\circ$. We use our previous measurement of the angle between the transition dipole moment and the permanent dipole moment of about 30°.[14] Note that in the recent paper of Brouard *et al.*[34] the authors proposed the transition dipole moment made an angle of 65°–80° to the linear OCS axis. For the analysis reported here we assume that our measurement with oriented molecules is interpreted correctly[14] and we extract from the observed angular distribution of the CO(J) fragment the "true" β parameter, β_{true}, using $\alpha_d = \chi + 30^\circ$. In Table 1 we show the values for the "experimental" β parameter, β_{exp}, without the correction of the influence from the parent alignment for several rotational states of the CO photofragment. The experimentally measured laboratory frame anisotropy parameters, β_2, β_4 and β_6 presented in Table 1, were fit using a nonlinear fitting algorithm[66] to expressions resulting from the coordinate frame transformation of eqn (1) to determine the molecular frame polarization parameters $a_q^{(k)}$. The 5 different laser geometries used for both ^{1}P$_1$ and ^{1}F$_3$ resonant intermediates provide us with a system of 10 equations and we have 6 unknown $a_q^{(k)}$ moments. To improve the quality of the fitting we also let the β parameter vary from the value β_{true} measured on single CO(J) states after correction for the small alignment of the parent state using eqn (3). The algorithm fitted the best $a_q^{(k)}$ values for a particular S-speed (correlating to a single J_{CO} cofragment) by minimizing $\chi^2 = \sum_g \sum_l \frac{(\beta_{l,\text{observed}} - \beta_{l,\text{calculated}})^2}{\delta^2_{l,\text{observed}}}$; l = 2,4 and 6; g labels the different polarization geometries; $\delta_{l,\text{observed}}$ is the estimated error in the measured parameters $\beta_{l,\text{observed}}$, which was taken to be 0.1 for all data. Note that we are only interested in relative changes of χ^2 as the absolute

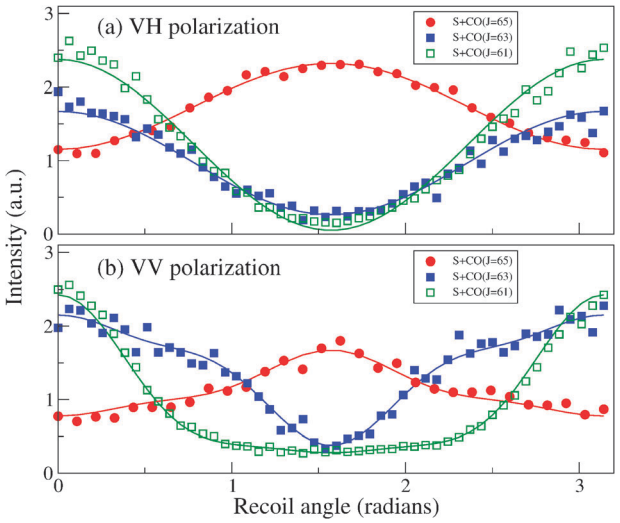

Fig. 4 The angular intensity distribution of $S(^1D_2)$ fragments as extracted from individual rings which are assigned to correlated single rotational states of the CO(J) cofragment: open squares CO(J = 61), solid squares CO(J = 63), and solid circles CO(J = 65), from photolysis of OCS(v_2 = 1|JlM = 111) at 42 594 cm^{-1} and detection of $S(^1D_2)$ *via* the $^1P_1$ intermediate state with either VH (panel a) or VV (panel b) polarization geometry. The individual angular distributions were fitted to a function $I(\theta) \propto (1 + \beta_2 P_2\theta)$ for the VH laser polarization geometry and to a function $I(\theta) \propto (1 + \beta_2 P_2\theta + \beta_4 P_4\theta + \beta_6 P_6\theta)$ function for the VV laser polarization geometry. The fits are shown as solid lines and the best fit coefficients β_n are given in Table 1. The angular distribution is extracted over a velocity band centered at the specific velocity peak of the radial velocity distribution as determined from images similar to the ones shown in Fig. 3 with a width of 10–16 pixels.

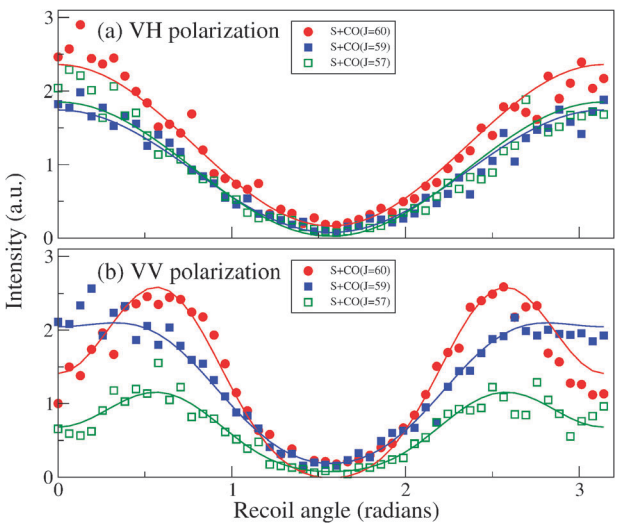

Fig. 5 Similar to Fig. 4 but different $S(^1D_2)$ fragments were selected in individual rings assigned to CO(J) cofragment: open squares CO(J = 57), solid squares CO(J = 59), and solid circles CO(J = 60). Otherwise as in Fig. 4.

value of χ^2 is determined by the estimated error in the experimental data. In a few cases it was observed that the fit algorithm was producing $a_q^{(k)}$ parameters beyond a physical maximum and in those cases we constrained such an $a_q^{(k)}$ parameter to the maximum physical value.

V. Discussion and conclusions

A One-surface *versus* two-surface dynamics

Theoretical calculations by Suzuki *et al.*[22] indicate that in the high J-region of the bimodal distribution the fragments are produced from parent molecules excited to a single parallel surface, $2^1A'(1^1\Delta)$. Very recently, Brouard and coworkers[34] concluded after studying the OCS photolysis at 248 nm that the excitation to the $2^1A'(1^1\Delta)$ electronic state is predominant and the excitation to the $1^1A''(1^1\Sigma^-)$ state is minor. However, the most recent *ab initio* theoretical study on OCS by Danielache *et al.*[38] report that near the peak of the absorption band at 223 nm the $2^1A'$ and the $1^1A''$ surface have an equal absorption strength for OCS at room temperature. For excitation wavelengths more towards the red the contribution of the $2^1A'$ surface is larger than the $1^1A''$ surface. Still, at an excitation of 42 594 cm^{-1} (234 nm) the recent theoretical work suggests that the relative contribution of $2^1A'$ *versus* $1^1A''$ is about 1 : 0.7, so a very large contribution of the perpendicular excitation to the $1^1A''$ surface.[38] Therefore, one of our goals is to determine whether our data can be explained with a one-surface dissociation model, at least for certain values of J, or whether a two-surface model is necessary.

We fit the angular distributions of the $S(^1D_2)$ photofragments with a single-surface model, described in ref. 51. The results of the fitting, the $a_q^{(k)}$ polarization parameters and the β parameter, are given in Table 2. We note that this model includes the effects of alignment of the OCS(v_2 = 1|JlM = 111) parent molecules, which, however, were predicted to be small for our experimental geometry with the orientation field perpendicular to the detector plane. We checked this prediction, by fitting the data with the one-surface model without parent-molecule orientation (by setting the orientation and alignment parameters $c_1 = 0$ and $c_2 = 0$) and verified that the results were very similar to the fitting that included parent-molecule orientation. Observing the fit parameters in Table 2, we notice that the results fit into two categories. In the first category, for J = 62–65 the quality of the fits is excellent and the value of χ^2 is very low. Note that when $\chi^2 = 10$ all calculated β parameters differ (on average) from the experimental β values by an estimated error of 0.1. All the fit parameters (the $a_q^{(k)}$ and β parameters) yield values within the physical ranges.[4] In the second category, for J = 57–61 (except J = 59) the quality of the fit appears to be worse (the value of χ^2 is about ten times larger) and some of the fit parameters (in particular the $a_1^{(2)}$ and $a_2^{(2)}$ parameters) yield values that are beyond the physical ranges. In the fit they were constrained to remain within the physical ranges (values shown in bottom row of Table 2). We interpret this behavior to mean that the dissociation dynamics, for J = 62–65, can be qualitatively described by singe-surface dissociation, whereas for J = 57–61 dynamics on more than one surface may become more important.

To test the need to include more than one surface in the dynamics, we fitted our data also to a two-surface model,

Table 1 Experimentally observed β_2, β_4 and β_6 Legendre polynomial coefficients of the angular distribution of $S(^1D_2)$ photofragments correlating with single rotational states, J_{CO}, of the CO cofragment (first column) after photolysis of $OCS(v_2 = 1|JlM = 111)$ at 42 594 cm^{-1}. The second column contains the calculated speed of $S(^1D_2)$ using the dissociation energy D_0 = 34 608 cm^{-1} determined before[32] and using conservation of linear momentum and energy in the two-body breakup of a single $OCS(v_2 = 1|JlM = 111)$ state with a spectroscopically accurate internal energy of 520.603 cm^{-1}. The rotational energy of CO(J) was calculated using the rotational constants reported before.[27] The third collumn contains the value of the anisotropy parameter $\beta_{exp}(J_{CO})$ as measured in a separate two-laser experiment with photolysis at 42 594 cm^{-1} and a probe laser around 230 nm detecting a single rotationally quantum state-selected CO(J) cofragment. The $\beta_{exp}(J_{CO})$ reported is the value directly obtained from the angular distribution of the slice image of CO(J), without the small correction for the alignment of the parent $OCS(v_2 = 1|JlM = 111)$ state, see eqn (3). The laser polarization geometry of photolysis and probe laser (V = vertical = in the slice imaging plane, H = horizontal = perpendicular to the slice imaging plane) and the resonant intermediate state used for detecting the $S(^1D_2)$ fragment are given in the first row.

			VV ($^1P_1$)			VH ($^1P_1$)	HV ($^1P_1$)		VV ($^1F_3$)			VH ($^1F_3$)
J_{CO}	$v(S^1D_2)$/m s^{-1}	$\beta_{exp}(J_{CO})$	β_2	β_4	β_6	β_2	β_2	β_4	β_2	β_4	β_6	β_2
65	359	−0.66	−0.47	0.09	−0.12	−0.41	0.18	−0.02	−0.49	−0.05	−0.06	−0.65
64	462	0.31	0.09	0.33	0.38	0.72	0.68	0.03	0.24	−0.01	0.07	0.37
63	545	0.79	0.94	−0.38	0.24	1.28	0.67	−0.45	0.80	−0.14	0.00	1.02
62	616	1.20	1.62	0.31	0.01	1.58	0.59	−0.08	1.29	0.01	0.00	1.51
61	678	1.44	1.58	1.05	0.44	1.88	0.85	0.46	1.38	0.14	0.08	1.46
60	734	1.31	1.39	−0.90	−0.53	1.64	0.65	−0.50	1.30	−0.37	−0.14	1.70
59	786	1.37	1.51	−0.31	0.17	1.77	0.60	−0.21	1.32	−0.32	−0.06	1.74
58	834	—	1.50	−0.94	−0.68	1.46	0.55	−0.32	1.26	−0.55	−0.01	1.66
57	878	—	1.45	−0.76	−0.47	1.93	0.49	−0.02	1.57	−0.16	0.00	1.82
Peak low $J \approx 47$	—	0.53	0.76	−0.31	0.50	0.83	0.61	0.27	0.14	−0.04	0.72	

Table 2 Best fit alignment parameters for photolysis at 42 594 cm^{-1} of an orientated $OCS(v_2 = 1|JlM = 111)$ parent molecule, assuming that the dynamics evolves on a single potential energy surface and including the effect of nonaxial recoil. The single rotational state, J_{CO}, of the CO cofragment, born in coincidence with the measured $S(^1D_2)$ photofragment at that velocity, is indicated in the first column. The experimental value of $\beta_{true}(J_{CO})$ using the experimental value $\beta_{exp}(J_{CO})$ (see Table 1) and applying eqn (3) (see also text), is given for comparison in the second column. The best fit $\beta_{fit}(J_{CO})$ and $a_q^{(k)}$ alignment moments are given in columns 3–9. The physical ranges of the parameters are given in the bottom row.

J_{CO}	$\beta_{true}(J_{CO})$	$\beta_{fit}(J_{CO})$	a_0^2	a_1^2	a_2^2	a_0^4	a_1^4	a_2^4	$\chi^2 - error^b$
65	−0.74	−0.58	−0.073	0.004	−0.37	0.0	−0.031	0.003	0.8
64	0.14	0.34	−0.28	−0.078	−0.42	−0.044	0.077	0.064	1.4
63	0.66	1.06	−0.46	−0.29	−0.46	0.046	0.076	0.014	1.5
62	1.06	1.42	−0.34	−0.33	−0.17	−0.033	−0.006	0.069	1
61	1.38	1.42	−0.28	−0.32	−0.59	−0.13	0.032	0.10	8
60	1.25	1.63	−0.57	−0.612[a]	−0.612[a]	0.12	0.00	−0.066	12
59	1.30	1.71	−0.57	−0.612[a]	−0.49	0.044	0.12	−0.023	1.5
58	1.65	1.62	−0.65	−0.612[a]	−0.612[a]	0.12	−0.036	−0.10	19
57	1.80	1.77	−0.40	−0.612[a]	−0.612[a]	0.082	0.012	−0.077	23
Physical range	−1 to +2	−1 to +2	−1 to +1	−1 to +1	−0.612 to +0.612	−0.167 to +0.25	−0.15 to +0.15	−0.1 to 0.127	

[a] Constrained in fit to the minimum physical value. [b] The $\chi^2 - error$ in the fit was calculated assuming an error in the experimental β_n coefficients of 0.1.

Table 3 Resulting best fit parameters for photolysis of $OCS(v_2 = 1|JlM = 111)$ at 42 594 cm^{-1} assuming that the dynamics evolves on two surfaces. The single rotational state, J_{CO}, of the CO(J) cofragment, born in coincidence with the measured $S(^1D_2)$ photofragment, is indicated in the first column. The corrected experimental value of $\beta_{true}(J_{CO})$, as extracted from the experimental $\beta_{exp}(J_{CO})$ (see eqn (3)), is given in the second column. The best fit $\beta_{fit}(J_{CO})$ and $A_q^{(k)}$ alignment moments are given in columns 3–11. The physical ranges of the $A_q^{(k)}$ parameters were calculated using eqn (16) in ref. 50 are given in the bottom row. Note that the maximum values of $A_q^{(k)}$ are given assuming the $a_q^{(k)}$ of both contributing surfaces are equal and maximum

J_{CO}	$\beta_{true}(J_{CO})$	$\beta_{fit}(J_{CO})$	A_0^2iso	A_0^2aniso	A_0^4iso	A_0^4aniso	A_1^2	A_2^2	A_1^4	A_2^4	$\chi^2 - error$
65	−0.74	−0.56	−0.13	−0.006	0.25	−0.063	−0.073	0.003	0.262	−0.018	1.9
64	0.14	0.50	−0.28	−0.033	0.11	−0.043	0.23	0.11	−0.019	0.025	0.5
63	0.66	1.05	−0.14	0.37	0.25	0.17	0.138	0.026	0.10	0.032	2.5
62	1.06	1.47	−0.11	−0.018	0.074	0.12	−0.009	0.032	−0.20	−0.019	1.8
61	1.38	1.57	−0.16	−0.088	0.093	0.012	0.091	0.44	−0.44	−0.11	36
60	1.25	1.48	−0.10	0.088	0.12	0.28	0.003	0.032	−0.087	0.16	13
59	1.30	1.68	−0.23	0.037	0.16	0.27	0.17	0.015	−0.35	0.074	2.6
58	1.65	1.47	−0.36	0.12	−0.046	0.38	−0.044	0.038	−0.63	0.24	24
57	1.80	1.68	0.087	0.061	0.20	0.14	0.026	0.032	0.10	0.14	6
Range	−1 to +2	−1 to +2	−1 to +1	−2 to +2	−3.0 to +3.0	−3 to +3	−0.167 to +0.25	−0.334 to +0.5	−0.723 to +0.723	−0.484 to +0.622	

[a] The $\chi^2 - error$ in the fit was calculated assuming an error in the experimental β_n coefficients of 0.1.

described by eqn (1) in ref. 51. The results of the two-surface model fitting (the $A_q^{(k)}$ and β parameters) are given in Table 3. We note that the difference between this two-surface model and the one-surface model used before is the addition of two q = 0 parameters for a total of four, the $A_0^{(k)}$(iso) and the $A_0^{(k)}$(aniso) for k = 2 and 4, instead of just two parameters, the $a_0^{(k)}$ for k = 2 and 4 in the one-surface model; these four q = 0 parameters allow the determination of two distinct m-state distributions of the S(^{1}D$_2$) photofragments, which are associated with dissociation *via* each of two distinct dissociative states. However, we note that this two-state model does not take into account the OCS(v_2 = 1|J|M = 111) parent-molecule orientation. Observing the fit parameters in Table 3, we notice that the two-state model does not fit the data significantly better than the one-state model (*i.e.* the χ^2 values of the fits are not significantly better, on average). The two-surface fit follows the similar trend of fitting the distributions well in the range J = 62–65, and less well for the range J = 57–61. The form of eqn (1) should fit any photofragment polarization angular distribution formed from the photodissociation of molecules *via* the coherent excitation of multiple dissociative states (*i.e.* including interference effect), provided that the parent molecules are not oriented or aligned. In addition, in ref. 51 it was shown that eqn (1) fits well the photofragment angular distribution from the photodissociation of oriented and aligned parent molecules, provided only single-surface (incoherent) terms are present. Perhaps, a possible reason for the failure of the single-surface model to fit the distributions in the range J = 57–61, and the failure of the two-surface model from eqn (1) to improve the fits is due to the presence of interference terms in the polarization of the S(^{1}D$_2$) photofragments from the coherent excitation of at least two dissociative states. These interference terms are not properly modeled by eqn (1), because the parent-molecule alignment has not been taken into account. However, because the degree of alignment of the OCS(v_2 = 1|J|M = 111) state is rather small in our experimental geometry, we wonder if such interference terms will be significant enough to influence the angular dependence in a more extended theoretical modeling of the angular dependence of the S(^{1}D$_2$) photofragment distribution. We note that our treatment of the OCS parent-molecule polarization deals only with the semiclassical alignment of the OCS dipole moment, and does not treat any effects of parent molecule angular momentum polarization on the photofragment polarization. Therefore, a full treatment, including the parent-molecule alignment for coherent excitation of multiple dissociative states and the correlation of parent and photofragment angular momentum, may allow the analysis of our results to yield further insight, especially for the product distributions with J = 57–61. Furthermore, perhaps there is also a connection with the strong changes in intensity of the CO(J = 61) + S(^{1}D$_2$) channel and the modeling of the angular distribution.

B *m*-State distribution and long-range potential

The m-state distributions were calculated from the angular momentum alignment moments $a_q^{(k)}$.[48] The population of the magnetic levels m_J for S(^{1}D$_2$) are given graphically in Fig. 6.

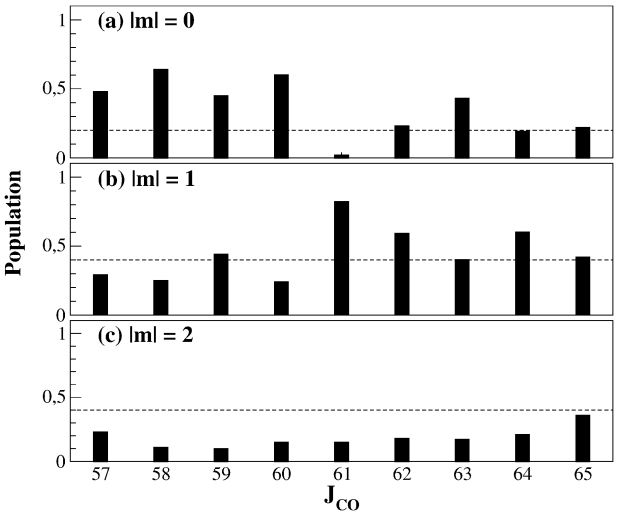

Fig. 6 S(^{1}D$_2$) m-state population for individual S($^1D_2$) + CO(J) dissociation channels in the high J region. The m-state populations where extracted from the one-surface model. The horizontal dashed line represents the statistical population in the absence of anisotropy.

As can be seen there is no clear trend of the m-state distribution with CO(J) level. We do see that for all J levels the population in m = 2 is significantly below the statistical population of 40% indicated by the dashed line in Fig. 6. The data suggest that for J levels smaller than J = 60 the m = 0 population is significantly above the statistical level and is ranging around 0.4 to 0.5. For high J-levels J = 62–65 the population in m = 0 is around 0.2, close to the statistical value. The S(^{1}D$_2$) distribution correlating with J = 61 appears very different, a large amount of population in m = 1 is found, about 80%.

At this moment there are no *ab initio* quantum calculations available to compare with the experimentally observed m-state distribution. Teule *et al.*[7] introduced a long-range model to interpret the m-state distribution in the O(^{1}D$_2$) fragment produced in the photodissociation of state-selected N_2O. This long-range model assumes that the distribution is determined, at some critical distance between the fragments, by the population eigenvalues of the 5 limiting surfaces correlating adiabatically with the ^{1}D$_2$ atomic quadrupole-diatomic dipole plus quadrupole potentials. In Fig. 7 we have plotted the m-state distribution as a function of the Jacobi OC–S bending angle for the ground state 1^1A′ surface and the 2^1A′, which is the excited state surface of relevance for the dynamics leading to the CO(J) + S(^{1}D$_2$) photofragments in the high J region.[22] Furthermore, we also plot the m-state distribution of the anti-symmetric 1^1A″ surface in Fig. 7.

We estimate that the deflection angle $\alpha_d = \chi_{fit} + 30°$, as obtained from the best fit χ_{fit} (see Table 2) ranges from about 46° for J = 57 to 98° for J = 65. As can be seen in panel (b) of Fig. 7 (2^1A'surface) in this bending angle region the m = 2 population is pretty flat around 0.1–0.2. In the same panel (b) we see that the m = 0 population is decreasing and the m = 1 population is increasing with increasing bending angle. Although the m = 0 and m = 1 populations do not show a very strong change we do see a similar trend with increasing deflection angle to somewhat lower m = 0 population and somewhat larger m = 1 population. The m-state populations

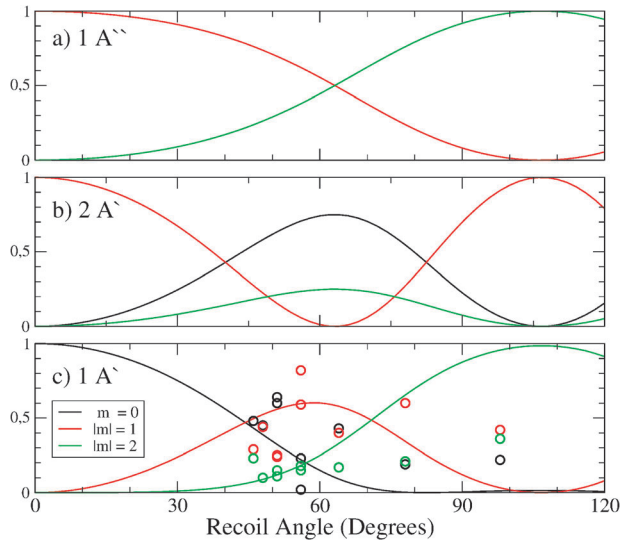

Fig. 7 The *m*-state populations obtained from diagonalizing the quadrupole–(dipole plus quadrupole) long-range OCS potential as a function of the OC–S Jacobi bending angle at a distance $R = 6$ Bohr between the CO and O fragment. In the top panel (a) the *m*-state populations on the $1^1A''$ surface are plotted, in the middle panel (b) the *m*-state populations on the $2^1A'$ surface, and in the bottom panel c) the *m*-state populations on the ground state $1^1A'$ surface. The corresponding colored circles in panel (c) are the experimentally observed populations in $m = 0$ (black circle), $|m| = 1$ (red circles) and $|m| = 2$ (green circles). The angle that is taken for the particular *J*-state is the total molecular frame deflection angle $\alpha_d = \chi_{fit} + 30^\circ$ as obtained from the best fit χ_{fit}, see Table 2.

on the long-range potential of the ground state surface, panel (c) of Fig. 7, shows a different behavior. Both the $m = 0$ and $m = 1$ populations are decreasing and the $m = 2$ population is strongly increasing for bending angles between 50–90°.

We notice that the $J = 61$ peak is anomalously strong in Fig. 2 and also the *m*-state distribution is striking with a very dominating $m = 1$ population of 80%. At this moment we can only speculate why this particular level may be special. It has been reported by Harich *et al.*[67] that for the photodissociation of HOD the centrifugal barrier leads to a very distinct rotational state population with about 50% of the population in a single rotational state $J = 28$. This effect is caused by a dynamically constrained threshold effect where $J = 28$ is the highest *J* level which is open *via* direct dissociation. The next few higher rotational channels which are energetically open are just below the centrifugal barrier. The photodissociation of water in the B-band is a highly anisotropic dissociation from a bent ground state potential to a linear excited state potential, whereas for OCS the excitation is from a linear ground state to a very bent excited state. We wonder if a similar accidental threshold behavior due to the centrifugal barrier may cause such an anomalous *J*-state distribution with a strikingly strong $J = 61$ level. We have done previously, see *e.g.* Fig. 7 in ref. 30, polarization experiments with a different photolysis wavelength around 230 nm and 223 nm. We did not see such a pronounced strong single rotational level as we observe here for photolysis near 42 594 cm^{-1} (234.7 nm). At present we are performing other experiments were we do a more targeted study to observe possible resonances in the absorption spectrum of OCS. Robert Wu and coworkers[37] measured the temperature dependence of the OCS absorption cross section. They observed very clear structure in the absorption spectrum between 200–240 nm, and this structure became more pronounced with decreasing temperature of OCS from 370 Kelvin to 170 K. These new studies are presently ongoing in our lab in Amsterdam and first indications are that indeed relatively sharp areas are observed in the absorption spectrum showing strong changes in the β-parameter of CO(*J*) in the highest *J*-channels just above the energetic threshold for dissociation. We intend to report these ongoing studies in the near future.

In conclusion, it would be extremely useful when novel theoretical dynamical calculations would become available to help interpret the rotational state dynamics, the correlated angular momentum polarization and other experimental results of the intriguing state-to-state photodynamics of OCS. We believe that such advanced quantum state-to-state calculations on the best *ab initio* potential energy surfaces available will help us to advance our understanding and interpretation of the novel experimental results presented here on our way towards performing the complete experiment.

Acknowledgements

This research has been financially supported by the councils for Chemical Sciences and Physical Sciences of the Dutch Organization for Scientific research (NWO-CW, NWO-FOM Atmospheric programme). We gratefully acknowledge further support of this project by financial support of the EU *via* the MarieCurie-ITN network ICONIC and the Integrated Infrastructure Initiative LaserLabEurope.

References

1 R. J. van Brunt and R. N. Zare, *J. Chem. Phys.*, 1968, **48**, 4304.
2 A. P. Clark, M. Brouard, F. Quadrini and C. Vallance, *Phys. Chem. Chem. Phys.*, 2006, **8**, 5591.
3 M. Brouard, R. Cireasa, A. P. Clark, F. Quadrini and C. Vallance, *Molecular Reaction and Photodissociation in the Gas Phase*, ed. P. D. Kleiber and K. C. Lin, Research Signpost, India, 2007.
4 A. Suits and O. S. Vasyutinskii, *Chem. Rev.*, 2008, **108**, 3706.
5 R. N. Zare and D. R. Herschbach, *Proc. I.E.E.E.*, 1963, **51**, 173.
6 R. Schinke, *Photodissociation Dynamics*, Cambridge University Press, Cambridge, 1995.
7 J. M. Teule, G. C. Groenenboom, D. W. Neyer, D. W. Chandler and M. H. M. Janssen, *Chem. Phys. Lett.*, 2000, **320**, 177.
8 M. Brouard, R. Cireasa, A. P. Clark, F. Quadrini and C. Vallance, *Phys. Chem. Chem. Phys.*, 2006, **8**, 5549.
9 D. W. Chandler and P. L. Houston, *J. Chem. Phys.*, 1987, **87**, 1445.
10 A. T. J. B. Eppink and D. H. Parker, *Rev. Sci. Instrum.*, 1997, **68**, 3477.
11 C. R. Gebhardt, T. P. Rakitzis, P. C. Samartzis, V. Ladopoulos and T. N. Kitsopoulos, *Rev. Sci. Instrum.*, 2001, **72**, 3848.
12 D. Townsend, M. Minitti and A. G. Suits, *Rev. Sci. Instrum.*, 2003, **74**, 2530.
13 J. Lin, J. Zhou, W. Shiu and K. Liu, *Rev. Sci. Instrum.*, 2003, **74**, 2495.
14 T. P. Rakitzis, A. J. van den Brom and M. H. M. Janssen, *Science*, 2004, **303**, 1852.
15 M. N. R. Ashfold, N. H. Nahler, A. J. Orr-Ewing, O. P. J. Vieuxmaire, R. L. Toomes, T. N. Kitsopoulos, I. A. Garcia, D. A. Chestakov, S.-M. Wu and D. H. Parker, *Phys. Chem. Chem. Phys.*, 2006, **8**, 26.

16 M. L. Lipciuc, J. B. Buijs and M. H. M. Janssen, *Phys. Chem. Chem. Phys.*, 2006, **8**, 219.
17 A. I. Chichinin, K.-H. Gericke, S. Kauczok and C. Maul, *Int. Rev. Phys. Chem.*, 2009, **28**, 607.
18 M. H. M. Janssen, D. H. Parker, G. O. Sitz, S. Stolte and D. W. Chandler, *J. Phys. Chem.*, 1991, **95**, 8007.
19 N. Sivakumar, G. E. Hall, P. L. Houston, J. W. Hepburn and I. Burak, *J. Chem. Phys.*, 1988, **88**, 3692.
20 G. Nan, I. Burak and P. L. Houston, *Chem. Phys. Lett.*, 1993, **209**, 383.
21 Y. Sato, Y. Matsumi, M. Kawasaki, K. Tsukiyama and R. Bersohn, *J. Phys. Chem.*, 1995, **99**, 16307.
22 T. Suzuki, H. Katayanagi, S. Nanbu and M. Aoyagi, *J. Chem. Phys.*, 1998, **109**, 5778.
23 Z. H. Kim, A. J. Alexander and R. N. Zare, *J. Phys. Chem. A*, 1999, **103**, 10144.
24 A. Sugita, M. Mashino, M. Kawasaki, Y. Matsumi, R. Bersohn, G. Trott-Kriegeskorte and K.-H. Gericke, *J. Chem. Phys.*, 2000, **112**, 7095.
25 T. P. Rakitzis, P. C. Samartzis and T. N. Kitsopoulos, *Phys. Rev. Lett.*, 2001, **87**, 123001.
26 A. J. van den Brom, T. P. Rakitzis, J. van Heyst, T. N. Kitsopoulos, S. R. Jezowski and M. H. M. Janssen, *J. Chem. Phys.*, 2002, **117**, 4255.
27 A. M. Rijs, E. H. G. Backus, C. A. de Lange, M. H. M. Janssen, N. P. C. Westwood, K. Wang and V. McKoy, *J. Chem. Phys.*, 2002, **116**, 2776.
28 A. J. van den Brom, T. P. Rakitzis and M. H. M. Janssen, *J. Chem. Phys.*, 2004, **121**, 11645.
29 M. Kim, W. Li, S. K. Lee and A. G. Suits, *Can. J. Chem.*, 2004, **82**, 880.
30 A. J. van den Brom, T. P. Rakitzis and M. H. M. Janssen, *J. Chem. Phys.*, 2005, **123**, 164313.
31 A. J. van den Brom, T. P. Rakitzis and M. H. M. Janssen, *Phys. Scr.*, 2006, **73**, C83.
32 M. L. Lipciuc and M. H. M. Janssen, *Phys. Chem. Chem. Phys.*, 2006, **8**, 3007.
33 M. L. Lipciuc and M. H. M. Janssen, *J. Chem. Phys.*, 2007, **126**, 194318.
34 M. Brouard, A. V. Green, F. Quadrini and C. Vallance, *J. Chem. Phys.*, 2007, **127**, 084304.
35 M. Brouard, F. Quadrini and C. Vallance, *J. Chem. Phys.*, 2007, **127**, 084305.
36 J. W. Rabalais, J. M. McDonald, V. Scherr and S. P. McGlynn, *Chem. Rev.*, 1971, **71**, 73.
37 C. Y. Robert Wu, F. Z. Chen and D. L. Judge, *J. Quant. Spectrosc. Radiat. Transfer*, 1999, **61**, 265.
38 S. O. Danielache, S. Nanbu, C. Eskebjerg, M. S. Johnson and N. Yoshida, *J. Chem. Phys.*, 2009, **131**, 024307.
39 T. P. Rakitzis, P. C. Samartzis and T. N. Kitsopoulos, *J. Chem. Phys.*, 1999, **111**, 10415.
40 S. K. Lee, R. Silva, S. Thamanna, O. S. Vasyutinskii and A. G. Suits, *J. Chem. Phys.*, 2006, **125**, 144318.
41 L. D. A. Siebbeles, M. Glass-Maujean, O. S. Vasyutinskii, J. A. Beswick and R. Octavio, *J. Chem. Phys.*, 1994, **100**, 3610.
42 M. Ahmed, E. R. Wouters, D. S. Peterka, O. S. Vasyutinskii and A. G. Suits, *Faraday Discuss.*, 1999, **113**, 425.
43 G. G. Balint-Kurti, A. J. Orr-Ewing, J. A. Beswick, A. Brown and O. S. Vasyutinskii, *J. Chem. Phys.*, 2002, **116**, 10760.
44 A. Smolin, O. S. Vasyutinskii, E. Wouters and A. Suits, *J. Chem. Phys.*, 2004, **121**, 6759.
45 V. V. Kuznetsov and O. S. Vasyutinskii, *J. Chem. Phys.*, 2007, **127**, 044308.
46 P. S. Shternin and O. S. Vasyutinskii, *J. Chem. Phys.*, 2008, **128**, 194314.
47 V. V. Krasilnikov, M. B. Kuznetsov, A. G. Suits and O. S. Vasyutinskii, *Phys. Chem. Chem. Phys.*, 2011, DOI: 10.1039/c0cp01375g.
48 T. P. Rakitzis and R. N. Zare, *J. Chem. Phys.*, 1999, **110**, 3341.
49 T. P. Rakitzis and A. J. Alexander, *J. Chem. Phys.*, 2010, **132**, 224310.
50 T. P. Rakitzis, *J. Chem. Phys.*, 2010, **133**, 204301.
51 T. P. Rakitzis and M. H. M. Janssen, *Mol. Phys.*, 2010, **108**, 937.
52 L. Bougas and T. P. Rakitzis, *Phys. Chem. Chem. Phys.*, 2010, DOI: 10.1039/c0cp02451a.
53 M. Brouard, A. P. Clark, C. Vallance and O. S. Vasyutinskii, *J. Chem. Phys.*, 2003, **119**, 771.
54 M. Brouard, R. Cireasa, A. P. Clark, T. J. Preston, C. Vallance, G. C. Groenenboom and O. S. Vasyutinskii, *J. Phys. Chem. A*, 2004, **108**, 7965.
55 M. Brouard, R. Cireasa, A. P. Clark, T. J. Preston and C. Vallance, *J. Chem. Phys.*, 2006, **124**, 64309.
56 A. M. Coroiu, D. H. Parker, G. C. Groenenboom, J. Barr, I. T. Novalbos and B. J. Whitaker, *Eur. Phys. J. D*, 2006, **38**, 151.
57 M. P. J. van der Loo, PhD Thesis, Radboud University, Nijmegen, 2008.
58 T. P. Rakitzis, *Chem. Phys. Lett.*, 2001, **342**, 121.
59 P. S. Shternin, V. K. Ivanov, A. Suits and O. S. Vasyutinskii, *Phys. Chem. Chem. Phys.*, 2006, **8**, 2972.
60 R. N. Dixon, *J. Chem. Phys.*, 1986, **85**, 1866.
61 T. P. Rakitzis, A. J. van den Brom and M. H. M. Janssen, *Chem. Phys. Lett.*, 2003, **372**, 187.
62 M. H. M. Janssen, J. W. G. Mastenbroek and S. Stolte, *J. Phys. Chem. A*, 1997, **101**, 7605.
63 M. L. Lipciuc, A. J. van den Brom, L. Dinu and M. H. M. Janssen, *Rev. Sci. Instrum.*, 2005, **76**, 123103.
64 M. L. Lipciuc, PhD Thesis, Vrije Universiteit, Amsterdam, 2008.
65 C. A. Taatjes, M. H. M. Janssen and S. Stolte, *Chem. Phys. Lett.*, 1993, **203**, 363.
66 W. Meerts and M. Schmitt, *Int. Rev. Phys. Chem.*, 2006, **25**, 353.
67 S. A. Harich, X. F. Yang, X. Yang, R. van Harreveldt and M. van Hemert, *Phys. Rev. Lett.*, 2001, **87**, 263001.